Conference paper

Mikhail G. Zuev*, Vladislav G. Il'ves, Sergey Yu. Sokovnin, Andrei A. Vasin and Elena Yu. Zhuravleva

New amorphous nanophosphors obtained by evaporation of silicates and germanates REE

DOI 10.1515/pac-2016-1118

Abstract: Amorphous nanophosphors have been produced by pulsed electron beam evaporation of bulk phosphors of rare earth elements (REE) silicates and germanates with oxyapatite structure activated with europium. The processes of crystallization of amorphous nanopowders (NP) have been studied by differential scanning calorimetry and thermogravimetry (40–1400 °C) methods. A modification of the Raman and IR spectra of the samples was found when the particle size decreased from bulk to nanostate due to insignificant polymerization of $Si(Ge)O_4$ tetrahedra. The spectral and luminescence characteristics of the bulk samples as well as nanoamorphous samples have been examined. It was established that Eu^{3+} forms two types of optical centers. Upon the transition of $Sr_2Gd_8(SiO_4)_6O_2$: Eu^{3+} phosphor from bulk state to nanostate during laser excitation, the luminescence intensity of Eu^{3+} ions increases 10 times. Blue and white amorphous nanophosphors have been obtained for the first time by evaporation of $Ca_2M_8(SiO_4)_6O_2$:Eu (M = Y, Gd) and $Ca_2La_8(GeO_4)O_2$:Eu phosphors. Radiation reduction of ions $Eu^{3+} \rightarrow Eu^{2+}$ in electron beam has been presumably found.

Keywords: Eu²⁺; Eu³⁺; luminescence; Mendeleev XX; nanophosphors; nanotechnology; synthesis; UV-visible spectroscopy; vibrational spectra; X-ray diffraction.

Introduction

The silicate matrices containing (REE) ions are known as effective phosphors showing promise, for example, for designing of LED devices [1–7]. There are numerous articles written on the topic of silicate nano- and bulk phosphors that contain Eu^{3+} and Eu^{2+} ions [8–12]. In many cases, nanophosphors are obtained by sol-gel processes.

In previous work [10], amorphous nanophosphors have been produced for the first time by pulsed electron beam evaporation (EBE) from polycrystalline phosphors $\mathrm{Sr_2Y_8}(\mathrm{SiO_4})_6\mathrm{O_2}$: Eu with the oxyapatite structure. The spectral luminescent characteristics of phosphors in polycrystalline and nanoamorphous states were examined. The cited work [11] provides a detailed description of the EBE method for the production of luminescent materials including silicate materials.

Article note: A collection of invited papers based on presentations at the XX Mendeleev Congress on General and Applied Chemistry (Mendeleev XX), held in Ekaterinburg, Russia, September 25–30, 2016.

Andrei A. Vasin: Institute of Solid State Chemistry, Ural Branch of Russian Academy of Sciences, 620990 Ekaterinburg, Russia Elena Yu. Zhuravleva: Ural Federal University, named after the First President of Russia B. N. Yeltsin 620002 Ekaterinburg, Russia

^{*}Corresponding author: Mikhail G. Zuev, Institute of Solid State Chemistry, Ural Branch of Russian Academy of Sciences, 620990 Ekaterinburg, Russia, e-mail: zuev@ihim.uran.ru

Vladislav G. Il'ves and Sergey Yu. Sokovnin: Institute of Electrophysics, Ural Branch of Russian Academy of Sciences, 620216 Ekaterinburg, Russia; and Ural Federal University, named after the First President of Russia B. N. Yeltsin 620002 Ekaterinburg, Russia

Furthermore, amorphous nanophosphors have been produced by EBE from bulk phosphors of the composition Sr,Gd_o(SiO_o)_cO_s:Eu, Ca,Y(Gd)_o(SiO_o)_cO_s:Eu and Ca,La_o(GeO_o)_cO_s:Eu. A modification of the IR and Raman spectra was detected, and the forbidden band width of the samples was found to increase when the particle size decreased from the bulk to the nanodimensional state. After the spectral luminescent characteristics in polycrystalline and nanoamorphous states have been studied, it was established that during transition to the nanoamorphous state some the phosphors have tendency to change their PL color from red-orange (Eu^{3+}) to blue (Eu^{2+}) .

Materials and methods

Nanopowders have been synthesized by the method of EBE evaporation on installation NANOBEAM-2 [12]; these targets made from stoichiometric bulk powders. The silicate bulk samples were synthesized by annealing of a mixture of the respective components in air. Bulk samples Sr(Ca),M_o(SiO_o),Eu (M=Y, Gd) have been synthesized by multistage annealing of a mixture of components. Synthesis was carried out in two stages. In the initial stage, 99.99% pure Sr(Ca)CO₂, M₂O₃, Eu₂O₃, and SiO₂ were used as the primary components to synthesize Sr(Ca), M_o(SiO_c), O_c and Sr(Ca), Eu_o(SiO_c), O_c. Stoichiometric amounts of these components were thoroughly mixed, and then the powders were annealed in the air at temperatures ranging between 1000 and 1400 °C with intermediate grinding of the charge. The total time of annealing was 80 h. In the second stage of the synthesis, an activating agent was added. For this purpose, the above compounds were taken in the stoichiometric ratio to obtain solid solutions of the composition $Sr(Ca)_2M_{8(1-x)}Eu_{8x}(SiO_4)_6O_2$. Thereafter, the thoroughly mixed substances were annealed in the air at 1450 °C for 20 h.

In order to synthesize Ca,La, (GeO,)O,:Eu, analytical grade reagents CaCO,, La,O, Eu,O, and GeO, were used as raw materials. Weighted samples of CaCO₃, La₂O₃ and Eu₂O₃ were dissolved in concentrated HNO₃. The GeO, solution was prepared in excess of NH₄OH. After the solution containing Ca(NO₃), La(NO₃), and Eu(NO₂), was placed into the ammonia solution of GeO₂, the resulting mixture was evaporated at 120 °C until a white precipitate was formed. The prepared material was then heat treated in several stages: the first stage includes heating from 200 °C to 800 °C with a step of 100 °C/h, the second stage includes sintering at 1000 °C for 14 h, and the third stage involves annealing at 1200 °C for 28 h.

The preparative methods of synthesis are analogous to those described in [13, 14].

Data analysis

The XPA was carried out on a Shimadzu XRD-7000 diffractometer (CuK_a radiation, CM-3121 counter monochromator, Scintillation Counter detector) using the ICDD card-file. The X-ray diffraction patterns of the produced samples were refined by the full-profile Rietveld method with the use of the ICDD card-file.

The specific surface area of the powders (S_{ss}) was determined by the Brunauer-Emmett-Teller (BET) method [15] on a Micromeritics TriStar 3000 device.

The thermal analysis of the NP was performed on a NETZSCH STA-409 thermal analyzer using thermogavimetry (TG) and differential scanning calorimetry (DSC) methods. The microscopic analysis of the NP was carried out a JEOL JEM 2100 transmission electron microscope. The IR-spectrum was measured by a Spectrum spectrophotometer (Perkin-Elmer) on powders suspended in nujol mull, while the Raman-spectra was measured on a Renishaw spectrometer ($\Delta v = 1000 \text{ cm}^{-1}$) using an argon laser at $\lambda = 514.5 \text{ nm}$ as an excitation source.

The absorption spectra were recorded on a UV-2401 PC device (Shimadzu) for the experimental estimation of the forbidden band width. The absorption edge was determined by extrapolation of the absorption coefficient linear dependence curve until it intersects the X-axis (wavelength). The intersection point determines the absorption edge.

The photoluminescence and excitation spectra were recorded respectively on an MDR-204 spectrometer (D lamp, R928 photomultiplier from Hamamatsu) and a Cary Eclipse fluorescence spectrophotometer (Xe pulse lamp with exceptionally long lifetime, pulsed at 80 Hz, pulse width at half peak height $2\,\mu$ s, peak power equivalent to 75 kW).

Results and discussion

X-ray phase analysis and microscopy

The solid solutions $Sr_2Gd_8(SiO_4)_6O_2$:Eu, $Ca_2Y(Gd)_8(SiO_4)_6O_2$:Eu and $Ca_2La_8(GeO_4)_6O_2$:Eu belong to the oxyapatite structure type. According to [13, 16] in crystals of oxyapatite (sp. gr. $P6_3/m$, z=1) in the designation of the Wyckoff the site-symmetry of atoms Y(Gd, La)1 - 4f, Sr(Ca) - 4f, Y(Gd, La)2 - 6h, Si(Ge) - 6h, O - 6h, O - 6h, O - 12i, O - 2a. Europium, replacing atoms of Y, Gd or Gd

Figure 1a shows a characteristic diffraction pattern of the synthesized solid solutions $Sr_2Gd_{6.53}Eu_{1.47}Si_6O_{26}$ (I), $Ca_2Y_{6.57}Eu_{1.43}Si_6O_{26}$ (II), $Ca_2Gd_{6.55}Eu_{1.45}Si_6O_{26}$ (III) and $Ca_2La_{6.4}Eu_{1.6}Ge_6O_{26}$ (IV). This composition was chosen because in the series of phosphors the solid solutions at the concentration of europium 0.2 mol has the maximum integral luminescence intensity of Eu^{3+} ions. At the concentration of europium more than 0.2 mol, concentration quenching of Eu^{3+} luminescence is observed. Processing by the Rietveld method yields the following data: single phase, sp. gr. $P6_3/m$. The characteristics of the obtained samples are given in the Table 1. The NP produced from this solid solution is X-ray amorphous (the characteristic X-ray diffraction pattern is shown in Fig. 1b).

Electron microscopy of the NP based on the sample (I) (Fig. 2a) reveals that the powder nanoparticles are strongly agglomerated and have an irregular shape tending to become quasispherical and are connected with each other by bridges of arbitrary length and shape (Fig. 2b). The electron diffraction data (Fig. 3a) and TEM HR pictures (Fig. 3b) show that the NP consists of amorphous particles only. The particle size in the

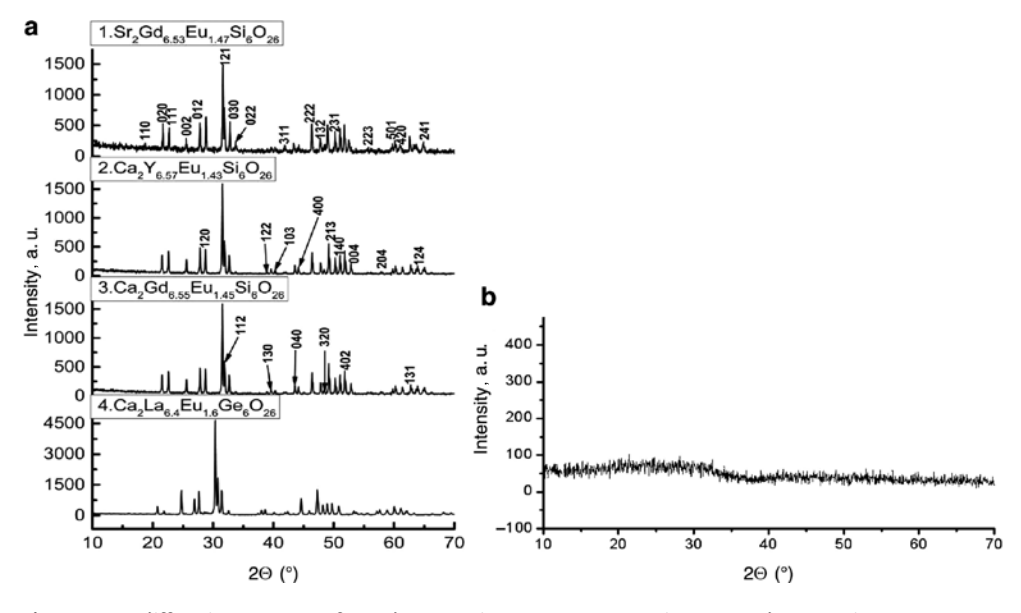


Fig. 1: X-ray diffraction patterns of $Sr_2Gd_{6.53}Eu_{1.47}Si_6O26$, $Ca_2Y_{6.57}Eu_{1.43}Si_6O_{26}$, $Ca_2Gd_{6.55}Eu_{1.45}Si_6O_{26}$, $Ca_2La_{6.4}Eu_{1.6}Ge_6O_{26}$ (a) and amorphous NP (b).

Table 1: Characteristics of the bulk samples obtained.

Sample no.	Composition	a, Å	c, Å	<i>V</i> , ų	Density, g/cm³
I	Sr ₂ Gd _{6 53} Eu _{1 47} Si ₆ O ₂₆	9.46889	6.97576	541.651	~6.19
II	$Ca_{2}Y_{6.57}Eu_{1.43}Si_{6}O_{26}$	9.34719	6.78283	513.220	~4.5
III	$Ca_{2}Gd_{6.55}Eu_{1.45}Si_{6}O_{26}$	9.41778	6.89690	529.763	~6
IV	Ca ₂ La _{6.4} Eu _{1.6} Ge ₆ O ₂₆	9.82131	7.16564	598.583	~5.7

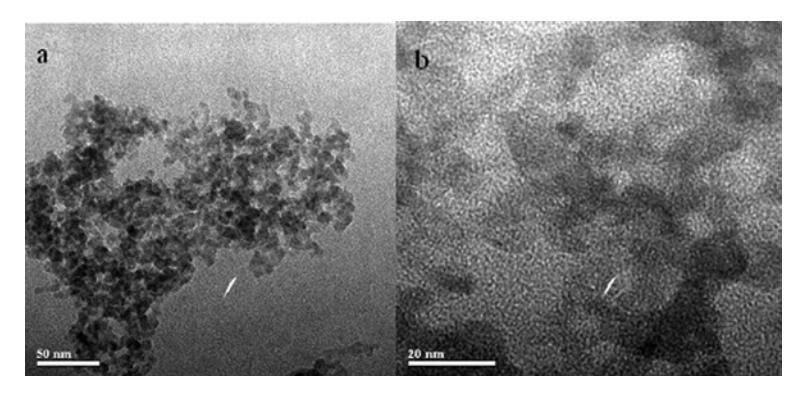


Fig. 2: A typical agglomerate of quasispherical NP particles (a) and TEM picture of bridges between quasispherical NP particles (b) based on $Sr_2Gd_{6.53}Eu_{1.67}Si_6O_{26}$.

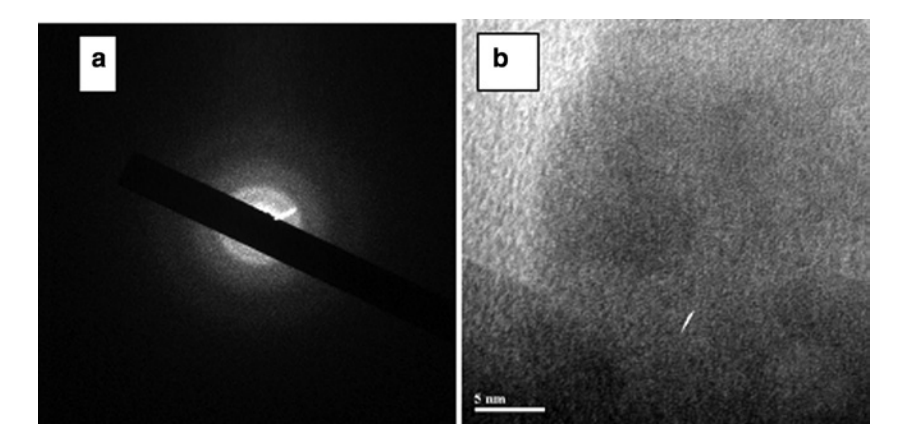


Fig. 3: Electron diffraction pattern of amorphous NP (a) and TEM HR-picture of amorphous NP based on $Sr_2Gd_{6.53}Eu_{1.47}Si_6O_{26}$.

NP generally does not exceed 20 nm. The BET value of the NP surface is $S_{sp} = 191.61 \text{ m}^2/\text{g}$. Consequently, the average NP particle size is 5 nm.

Electron microscopy of the NP (Fig. 4a) produced on the basis of $\text{Ca}_2\text{Y}_{6.4}\text{Eu}_{1.6}\text{Si}_6\text{O}_{26-8}$, where δ is oxygen non-stoichiometry, revealed that the nanoparticles are rather strongly agglomerated and have an irregular shape tending to form quasi-spherical particles and are connected with each other by nips of arbitrary length and shape. Oxygen nonstoichiometry appears due to the formation of Eu^{2+} ions (shown below). The data of electron diffraction analysis (the electron diffraction patterns were taken from six different regions of the sample, see the inset in Fig. 4a) and the TEM HR pictures (Fig. 4b) with different magnification confirm that the NP consists exclusively of amorphous particles. The BET value of the nanoparticle surface is $\text{S}_{\text{sp}} = 232.25 \text{ m}^2/\text{g}$; as a consequence, the average particle size is ~5.7 nm.

In addition to that, electron microscopy of the NP obtained on the basis of $Ca_2Gd_{64}Eu_{1.6}Si_6O_{26-\delta}$ (Fig. 5a) showed that the nanoparticles are also agglomerated. The agglomerates in the NP several hundred nanometers

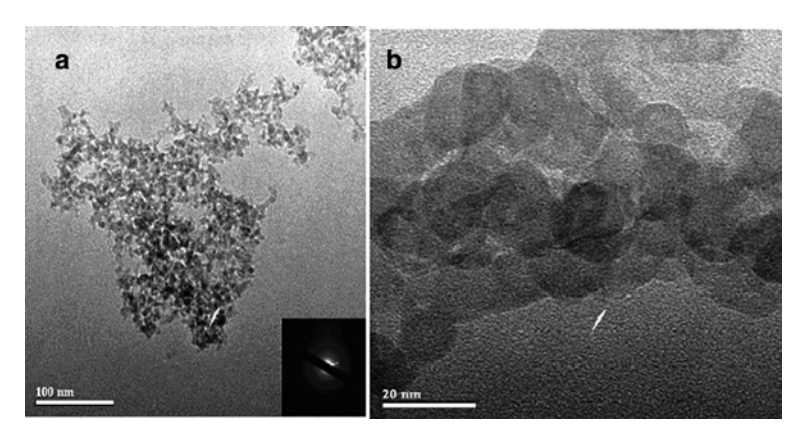


Fig. 4: The TEM pictures of the NP based on $Ca_2Y_{6.57}Eu_{1.43}Si_6O_{26}$: an agglomerate of nanoparticles (inset: the electron diffraction pattern of the amorphous region of the sample) (a); quasi-spherical amorphous nanoparticles (b).

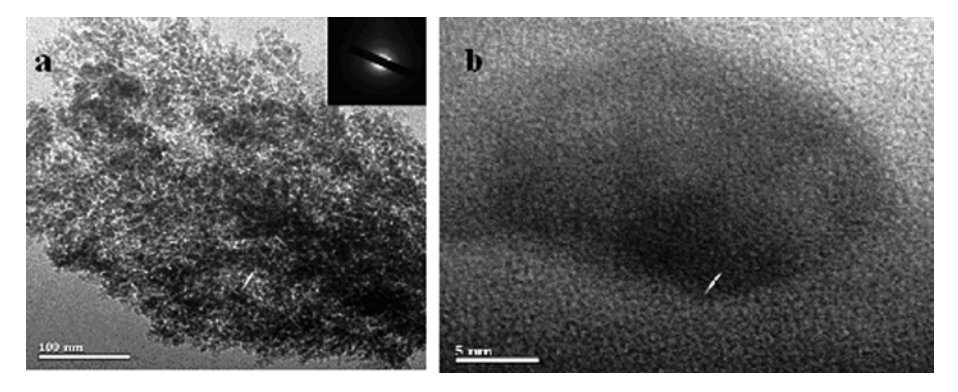


Fig. 5: The TEM pictures of the NP based on Ca₂Gd_{6.55}Eu_{1.65}Si₆O₂₆: a typical dendrite-like agglomerate of quasi-spherical nanoparticles (inset: the electron diffraction pattern of the amorphous region of the sample) (a); an image of a nanoparticle aggregate region (b).

in size generally have a dendrite-like shape and consist of irregularly-shaped nanoparticles prone to form quasi-spherical particles. The electron diffraction data and the TEM HR pictures demonstrated that the NP consists of amorphous particles only (Fig. 5b). The BET value of the nanoparticle surface is $S_{sp} = 172.63 \text{ m}^2/\text{g}$; as a result of it, the average particle size is 5.6 nm.

Just as in the previous three cases of microscopy, the sample (IV) reveals that the powder nanoparticles are strongly agglomerated and amorphous (Fig. 6). The BET value of the nanoparticle surface is $S_{sp} = 105.5 \text{ m}^2/\text{g}$. Consequently, the average particle size is 9.9 nm.

Thermal analysis

In order to characterize the obtained nanoparticles and to determine their thermal stability and the beginning of crystallization, we carried out DSC-TG analysis. The sample heating rate is 10 °C/min. In the temperature interval 50-500 °C the batch mass decreases by ~13 % owing to removal of water from NP and CO, release. Weak signals from water and carbon dioxide are found on the mass spectra in the temperature intervals 50-400 °C (H₂O) and 230-500 °C (CO₂). Adsorption of water and CO₂ on the nanoparticle surface can occur both directly during NP deposition in the evaporation chamber and after removal of the samples from the chamber since the highly-developed NP surface captures water and CO, vapors from ambient air. Crystallization of amorphous nanoparticles begins at a relatively low temperature and has probably two stages. At the

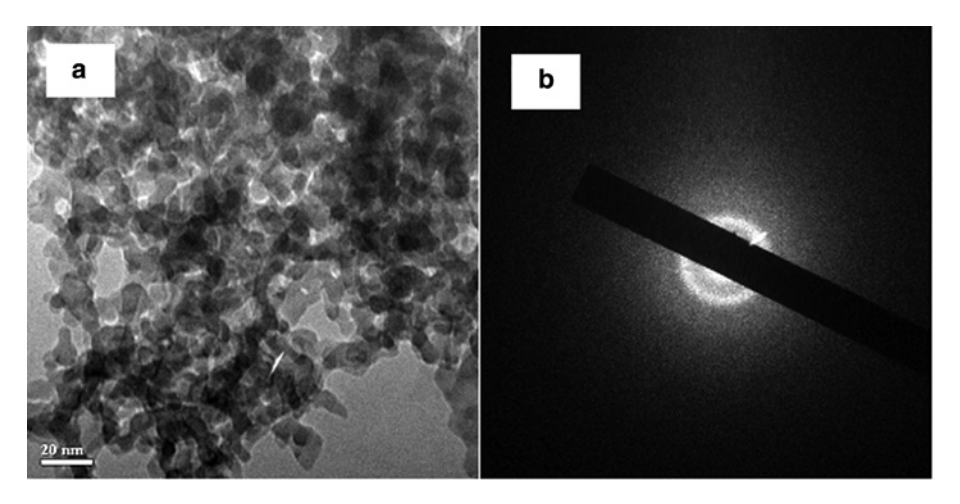


Fig. 6: The TEM pictures of the NP based on Ca, La, 4Eu, 6e, O,6: agglomerate of quasi-spherical nanoparticles (a); electron diffraction pattern of amorphous NP (b).

first stage, at temperatures from 200 to 400 °C, separate nanoparticles crystallize. Low thermal stability of the NP at this stage is likely to be due to the dimensional factor, since the size of the nanoparticles is ~5 nm. At the second stage (~800–970 °C) agglomerated nanoparticles crystallize [13].

For the sample based on NP (II) in the temperature range 50–1000 °C, the mass of the sample decreased by about 11.8% owing to removal of adsorbed crystal water and unknown carbon compounds from the NP. The signals from water and CO, are observed on the mass spectra in the temperature intervals 50-330 °C and 50-1000 °C, respectively Crystallization of amorphous nanoparticles begins at a low temperature as indicated by a strong exothermic peak in the temperature interval from 330 to 1000 °C. The low thermal stability of the NP is due to the effect of the nanoparticle size factor. CO, gas emission is completed simultaneously with termination of amorphous nanoparticle crystallization at about 1000 °C and is not observed further. During heating of the NP up to 1400 °C, a small increase in the sample's mass is observed (by 1.86 %), which is accompanied by three exothermic transformations of unknown nature associated with oxidation of nanoparticles.

For the sample based on NP (III) in the temperature interval from 50 to 1400 °C, an approximately 12.3 % mass loss is observed, which is due to removal of adsorbed and crystal water. The signals from water are detected on the mass spectrum in the temperature range ~50–330 °C. The crystallization of amorphous nanoparticles begins at ~1020 °C, as indicated by a strong extended exothermic peak on the DSC heating. The large length of exothermic points to a slow kinetics of amorphous NP transformation into crystalline powder (probably, the smallest amorphous nanoparticles begin to crystallize, as evidenced by the inflection of the DSC baseline curve at about 1020 °C). As the temperature increases up to 1080 °C, active crystallization of amorphous nanoparticles begins, which is reflected in the strengthening of heat generation terminating at about 1350 °C. Two insignificant thermal peaks observed on the DSC heating curve at ~860 and 940 °C can be associated either with sublimation of different organic compounds of unknown nature (except CO₂) from the nanoparticle surface or with a complex stepwise crystallization of amorphous nanoparticles having smaller dimensions.

For the sample based on NP (IV) in the temperature interval from 50 to 600 °C, an approximately 7.58 % mass loss is observed, which is due to removal of adsorbed and crystal water. In the temperature interval 600–760 °C, an approximately 0.5 % mass loss is observed. As the temperature increases up to 810 °C crystallization of amorphous nanoparticles begins. This is indicated by a small exothermic peak on DSC heating curve. As the temperature increases up to 870 °C, active crystallization of amorphous nanoparticles begins, which is reflected in the strengthening of heat generation terminating at about 1370 °C. As the NP is further heated up to 1400 °C, a dip of the DSC heating curve is observed suggesting the termination of amorphous NP crystallization.

Thus, according to the results of thermal analysis, individual amorphous nanoparticles obtained on the basis of samples I-IV are resistant at temperatures below the following numbers for each sample: I-200, II-330, III-1020, IV-810 °C.

Raman and IR spectroscopy

Raman spectra of sample I and amorphous NP based sample I are shown in Fig. 7a [13]. The frequencies v., v_3 , v_3 and v_4 of the internal vibrations of isolated SiO₄ tetrahedra are designated for the polycrystals. The spectrum of amorphous NP exhibits the formation of a structure, which is slightly different from that of the initial polycrystalline sample. The location of lines in the NP spectrum shows that it contains mainly isolated SiO₄ groups. At the same time the appearance of frequencies in the region 600–700 cm⁻¹ points to the formation of an inconsiderable concentration of polymerized silicon-oxygen fragments in the sample [17]. The frequency at 755 cm⁻¹ relating probably to vibrations of bridge bonds Si-O-Si is an indicator of the polymerization processes [17, 18]. In the process of evaporation of sample I and subsequent NP deposition on a glass substrate, the restructuring of the anionic motif of the silicate is likely to take place and display silicon-oxygen complexes with an insignificant concentration of SiO, tetrahedra. This phenomenon is analogous to the polymerization effect in rapid-quenched silicate melts of crystals with isolated complexes SiO. Oxygen ions that do not enter into the composition of the tetrahedra take part in this process. This is due to the presence of TR ions that can form partially covalent bonds with oxygen, for example, in Ca,Gd_o(SiO₄),O₃ [18]. The external vibration frequencies of SiO₄ shift towards the low-energy region (125–313 cm⁻¹). The shift of the line at 313 cm⁻¹ (E_x symmetry) is presumably due to the decrease in the force coefficient of the E_x component of the libration vibration of the SiO_a complex [18]. Besides, redistribution of intensities of external vibration lines is observed. The internal vibration frequencies also shift towards the low-energy region of frequency v_4 , and the intensity of the lines at v_1 and v_3 decreases considerably. These effects in the spectrum can be due to unification of a large number of oxygen vacancies in nanosample that emerge during evaporation of the bulk sample. The unification of vacancies breaks the translational symmetry. Such symmetry breakdown can cause the reduction of the intensity of the line at v. [19, 20].

Raman spectra of polycrystalline samples II and III and NP on their basis are depicted in (Fig. 7b and c). The spectrum of the amorphous NP produced by evaporation of II (Fig. 7b) shows the formation of a structure differing slightly from the structure of the initial polycrystalline sample. The position of the lines in the spectrum of the NP suggests that it contains mainly the isolated SiO₄ groups. The appearance of frequencies in the region of 600–700 cm⁻¹ bears witness to the formation of an insignificant concentration of polymerized silicon-oxygen fragments in the sample [13, 17]. The emergence of a new frequency at 716 cm⁻¹, which is likely to refer to vibrations of the Si-O-Si bridge bonds, is indicative of the polymerization processes [18]. Oxygen O(4) in the 2a position that does not enter into the compositions of SiO_4 tetrahedra probably participates in the polymerization process [13].

The frequency 138 cm⁻¹ is shifted into the high-frequency region and the frequencies of external vibrations of isolated SiO, complexes disappear (187–250 cm⁻¹ region). The shift of the line at 337 cm⁻¹ into the highfrequency region is presumably due to the increase in the force coefficient value of the E_{2g} component of the SiO_{M} complex libration vibration. The frequencies of internal vibrations v_{2} , v_{1} and v_{3} are also shifted into the high-frequency region. The frequency v_a , by contrast, is displaced into the low-frequency region. A relative decrease in the intensity of lines at v_1 and v_2 is observed. These effects in the spectrum can be induced by amalgamation of a large number of oxygen vacancies in the nanosample, which appear during evaporation of the sample and its further solidification. The amalgamation of vacancies leads to translational symmetry violation. Concurrently, such symmetry violation can cause the reduction of the intensity of the line at v. [19, 20].

The spectrum of amorphous NP produced by evaporation of III (Fig. 7c) has a structureless shape with no characteristic scattering lines. This can be also a result of translational symmetry violation in the NP and, consequently, complete lifting of the prohibition imposed by the quasi-momentum conservation law. As a result, phonons with any wave vectors are allowed [21].

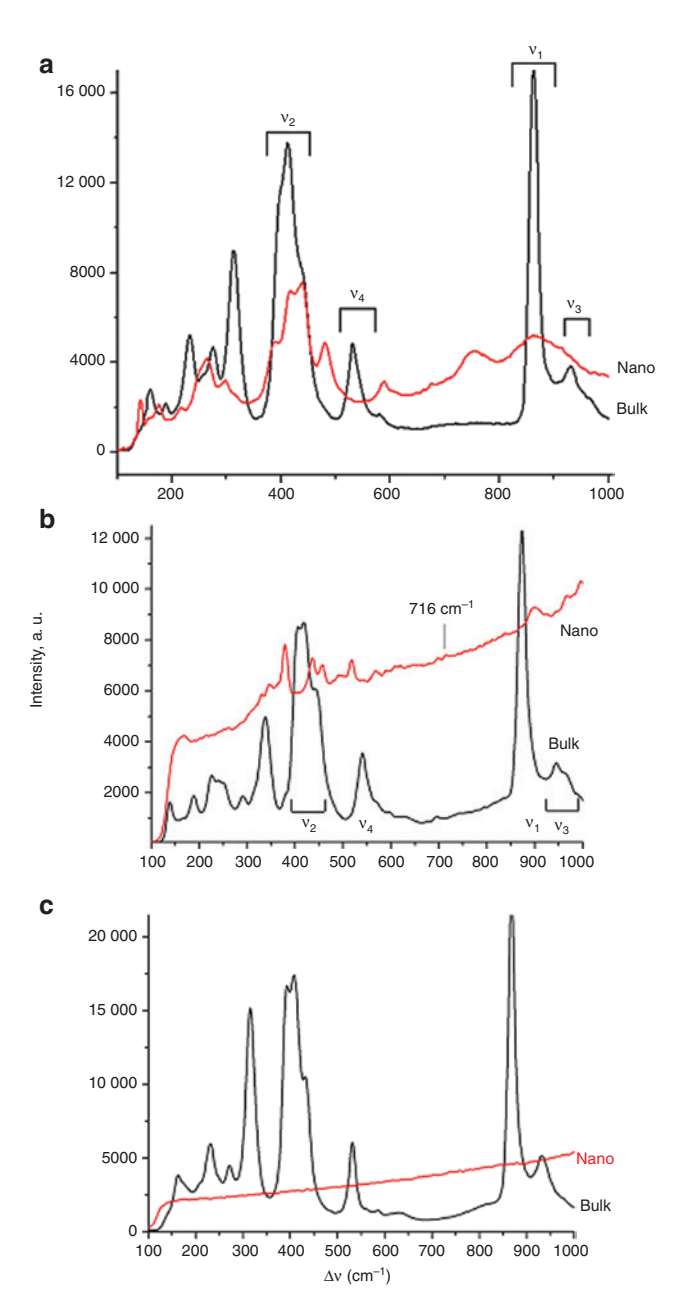


Fig. 7: Raman spectra of bulk and NP: $Sr_{y}Gd_{6.53}Eu_{1.67}Si_{6}O_{76}$ (a), $Ca_{y}Y_{6.57}Eu_{1.63}Si_{6}O_{76}$ (b), $Ca_{y}Gd_{6.55}Eu_{1.65}Si_{6}O_{76}$ (c).

The Raman spectra of $\text{Ca}_2\text{La}_{6,4}\text{Eu}_{1.6}\text{Ge}_6\text{O}_{26}$ and NP based thereon are not informative enough. Therefore the IR spectra of these samples have been analyzed (Fig. 8). Figure 8 displays the vibration frequencies v_2 , v_3 , v_4 of isolated tetrahedron GeO_4 [22, 23]. The absorption bands in the NP spectra are broadened which is indicative of disordering of GeO_4 groups. The spectrum of the amorphous NP points to the formation of a structure, which is somewhat different from that of the initial polycrystalline sample. The position of bands in the NP spectrum suggests that it contains mainly the isolated GeO_4 groups. A band is formed at 392 cm⁻¹, which corresponds probably to the frequency v_4 . The internal vibration frequency v_3 (789 cm⁻¹) of the GeO_4 groups is considerably shifted into the high-frequency region. A new band at 557 cm⁻¹ appears. This band corresponds to the Ge–O–Ge bridge vibrations [24] and is indicative of partial polarization of the GeO_4 groups. Oxygen ions that do not enter into the composition of the tetrahedra (oxygen O(4) in the 2a position) are involved in this process. During evaporation of sample IV and subsequent NP deposition on a glass substrate, restructuring

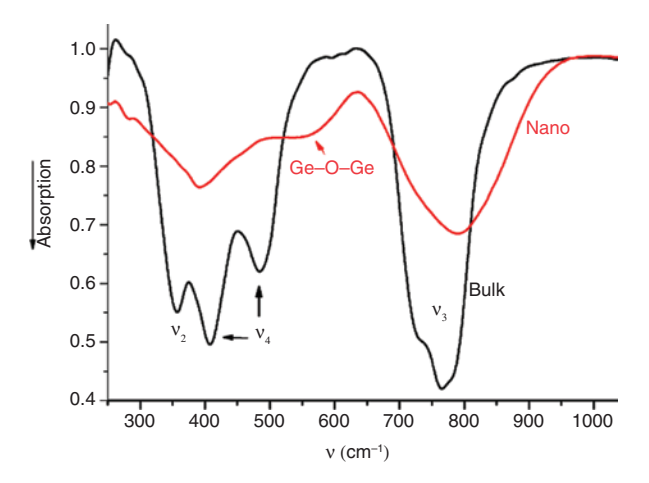


Fig. 8: IR spectra of sample Ca₂La₆, Eu_{1.6}(GeO₄), O₂ and NP at its base.

of the germanate anionic motif is likely to take place, and germanium-oxygen complexes with condensation of GeO, tetrahedra probably appear.

Optical spectroscopy chosen silicates

The Eu³⁺ photoluminescence spectra of the samples in the bulk phosphors and in nanophosphors (sample I) are displayed in Fig. 9a and b. Two lines for the transition ${}^5D_0 \rightarrow {}^7F_0$ for bulk and nanophosphor point to the formation of two types of optical centers formed by the Eu $^{3+}$ ions occupying the 4f and 6h positions in the silicate structure (similarly to $Sr_2Y_8(SiO_4)_6O_3$:Eu phosphors [25]).

Consider the effect of nanoparticle disordering on red photoluminescence purity of the samples. For this purpose, we determine the ratio of intensities of red "R" (${}^5D_0 \rightarrow {}^7F_1$ transition) and orange "O" (${}^5D_0 \rightarrow {}^7F_1$ transition) luminescence for bulk and nanophosphor. It is known that the electric dipole transition ${}^5D_0 \rightarrow {}^7F_2$ is supersensitive to site symmetry of Eu³⁺ ion in optical center. According to the selection rules, the $^5D_0 \rightarrow ^7F_1$ transition is allowed if Eu3+ ion in the optical center occupies a position that does not coincide with the inversion center. The magnetic dipole transition ${}^5D_0 \rightarrow {}^7F_1$ is also allowed. The R/O ratio is equal to 5.8 (bulk) and 6.1 (NP). Therefore, the intensity of red luminescence in the nanophosphor increases. As noted in work [26], this phenomenon is due to nanoparticle disordering providing relatively lower symmetry of electrostatic field around Eu³⁺ ions than in bulk phosphor and consequently a higher probability of the $^5D_0 \rightarrow ^7F_2$ transition. This will increase the intensity of red luminescence.

The essential difference in the bulk and nanophosphors is increased integral luminescence intensity for the NP. The intensity of electric dipolar transitions ${}^5D_0 \rightarrow {}^7F_2$ for the NP increases 10 times. The spectral lines for some agglomerated nanoparticles are broadened, which points to a disordered position of the optical centers in the NP.

Figure 9c-g shows the excitation spectra of optical luminescence centers in $Sr_2Gd_{6.5}Eu_{1.47}Si_6O_{26-\delta}$ polycrystals (c) and NP (e) in the interval $\lambda_{ex} = 250 - 360$ nm ($\lambda_{em} = 614$ nm). The excitation bands are due to the transition of Eu³⁺ to the charge-transfer state (Eu³⁺ \rightarrow O²⁻). Each band is a superposition of spectra of two optical centers. The maximum values of the excitation wave lengths are different for the bulk powder and NP. The maxima are located, respectively at $\lambda_{\text{max}}\!\approx\!269$ and 263 nm.

This difference in the wave length maxima of the charge transfer bands can be explained by different stability of the nearest oxygen ions O²⁻ surrounding Eu³⁺ ion. The influence of ligands on the charge transfer band was described in work [27]. The oxygen ions coordinating Eu³⁺ in the optical centers are stabilized predominately by the Si⁴⁺ ions. Apparently, the O²⁻ ions in nanophosphor are stabilized by surrounding positive ions to a somewhat greater degree than in bulk phosphor and therefore more energy is required to remove electron from these ions [27]. In this connection it can be expected that the charge transfer band in

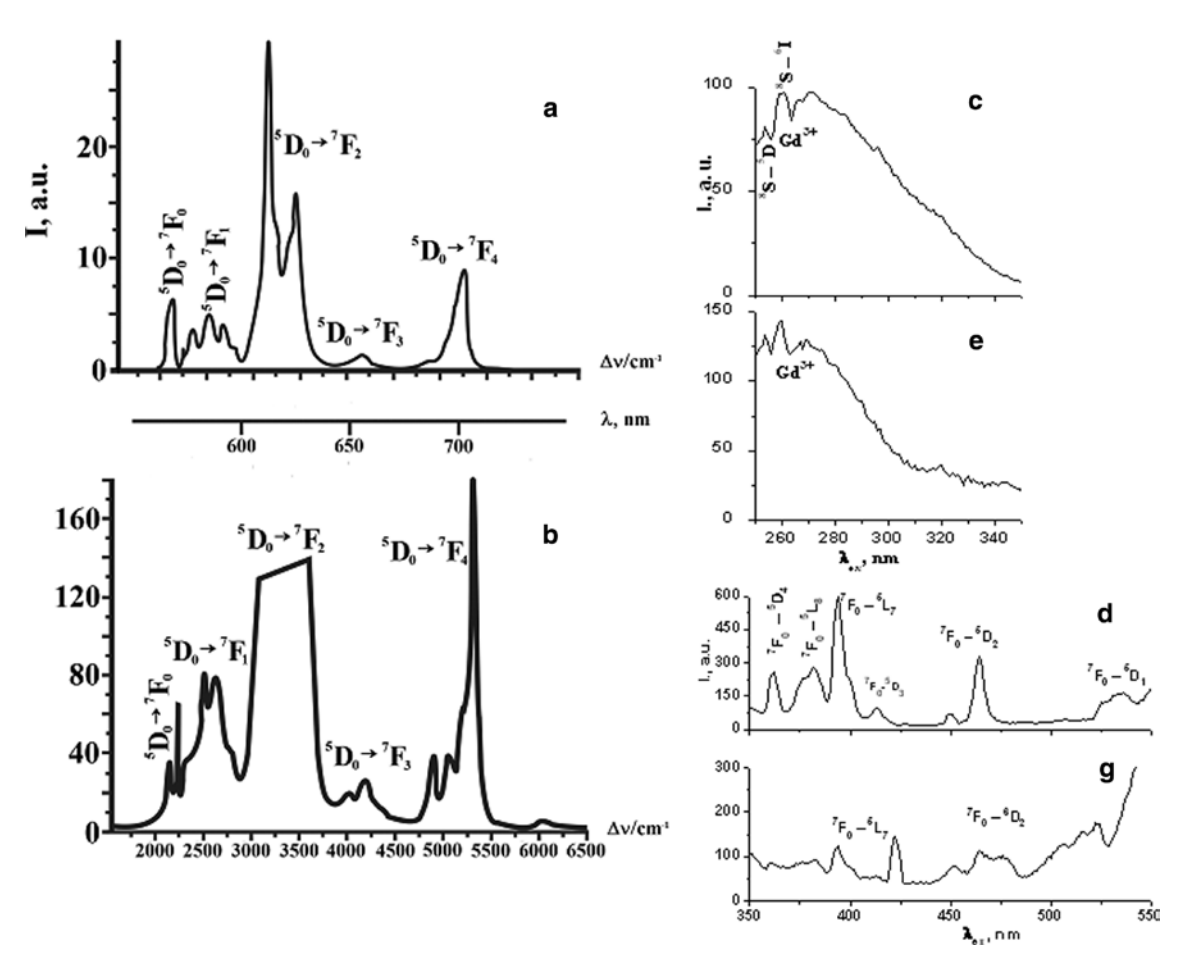


Fig. 9: PL spectra of samples bulk I (a), NP (b) and PLE spectra of bulk I (c, d), NP (e, g) ($\lambda_{em} = 614 \text{ nm}$).

nanophosphor will be shifted to the short-wave spectral region as compared with the analogous band in bulk phosphor. Besides, optical absorption (charge transfer transition) includes the oxygen p states. The p states are very sensitive to europium ion environment variation [28]. Consequently, this may suggest a slight variation of this environment in nanophosphor.

Figure 9c and e contain excitation bands corresponding to ${}^8S \rightarrow {}^5D$ and ${}^8S \rightarrow {}^6I$ transitions of Gd³+ ion. Therefore, a resonant transfer of excitation energy from the Gd³+ ions to the Eu³+ ions takes place in bulk and nanophosphors. An analogous transfer of excitation energy was observed in work [2].

Figure 9d and g also demonstrates the luminescence excitation spectra of the optical centers formed by the Eu³+ ions in the wave length interval λ_{ex} = 350–550 nm for the polycrystals (Fig. 9d) and NP (Fig. 9g). The spectra were recorded for λ_{em} = 614 nm. The excitation spectra of the bulk powder exhibit absorption lines of Eu³+ ions corresponding to the 5D_J and 5L_J transitions. Assignment of the transitions was carried out using the book [29]. The excitation spectra of the NP at λ_{em} = 614 nm exhibit Eu³+ ion absorption lines corresponding to the 5L_J and 5D_Z transitions. From comparison of Fig. 9d and g, it is seen that redistribution of intensities between sublevels of ${}^7F_0 \rightarrow {}^5D_Z$ transition takes place for bulk and nanophosphor. According to the selection rules, ${}^7F_0 \rightarrow {}^5D_Z$ is a supersensitive transition [30]. Therefore the redistribution of intensities is indicative of certain distortion of the local environment of Eu³+ ions in nanophosphor in comparison with bulk phosphor.

Consider the variation in the width of the forbidden band $\rm E_{\rm g}$ of the samples during transition from bulk powder to NP. Figure 10a presents the absorption spectra for $\rm Sr_2Gd_{6.52}Eu_{1.47}Si_6O_{26-8}$ and NP. The absorption edges are located, respectively at 354 and 304 nm. Consequently, in the transition from bulk to NP the value of $\rm E_{\rm g}$ increases from 3.50 to 4.08 eV. The absorption edge of phosphors is due to the absorption in the charge

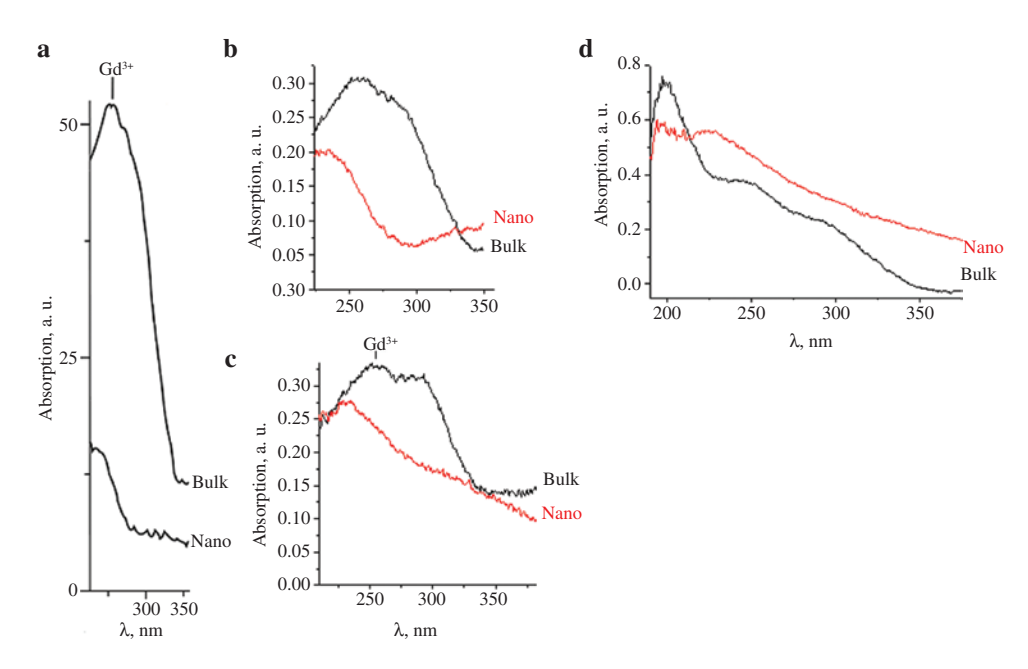


Fig. 10: Spectra of absorption of samples: I (a), II (b), III (c), IV (d).

transfer band (the $4f'2p^{-1}$ state) that is analogous to $Sr_2Y_{6,4}Eu_{1,6}(SiO)_6O_2$ phosphor [25]. The charge transfer level in Eu^{3+} forms the upper edge of the band. In bulk phosphors, the charge transfer level has a somewhat smaller energy than in nanophosphors. Therefore the fundamental absorption edge in nanophosphors is higher than in bulk phosphors. Consequently, along with different stability of the nearest oxygen ions O^{2-} surrounding Eu^{3+} ion in bulk and nanophosphor, we have to do here with small variation of this environment in nanophosphor. The environment of europium ions can be changed owing to insignificant concentration of SiO_a tetrahedra.

The band with a maximum at ~252 nm for bulk phosphor can be attributed to the ${}^8S \rightarrow {}^5D$ transition of Gd^{3+} ion [2].

What is the reason of the integral luminescence intensity increase for amorphous nanophosphor in comparison with polycrystalline silicate? This effect is considered in the model of optical centers in the configuration coordinates in [13].

Consider the variation in the forbidden band E_g width of the samples when going from bulk powder to NP. Figure 10b depicts the absorption spectra of bulk and NP samples. For sample of II, the absorption edge is at ~347.5 nm, while for the NP produced by evaporation of this silicate – at 294.5 nm (Fig. 10b). Consequently, in the transition from bulk to NP, the value of E_g increases from 3.567 to 4.209 eV. Figure 10c demonstrates the absorption spectra of the samples of III and NP based on this phosphor. For bulk phosphor, the absorption edge is at 365 nm, which corresponds to E_g = 3.396 eV. The band with a maximum at 256 nm can be attributed to the ${}^8S \rightarrow {}^5D$ transition of Gd^{3+} ion [2]. In the region of absorption boundary there is an extended exponential tail, the so-called Uhrbach tail, typical of amorphous media [31]. The Uhrbach tail allows one only to estimate the absorption boundary value. The absorption edge is at 367 nm (3.34 eV).

From the excitation spectra of Eu³⁺ ions it is seen (Fig. 11b) that the excitation band maximum in bulk phosphors II and III is equal to 270 nm (λ_{em} = 614 nm). For nanophosphors, the maximum is at λ_{ex} < 260 nm (Fig. 12b). Therefore in bulk phosphors the charge transfer level has a smaller energy than in nanophosphors. The fundamental absorption edge in nanophosphors should be higher than in bulk phosphors. Consequently, along with different stability of the nearest O²⁻ ions surrounding the Eu³⁺ ion in bulk and nanophosphors, it is possible to suggest a small variation in this environment in the nanophosphor.

Figure 11a exhibits the PL spectra of $Ca_2Y_{6.4}Eu_{1.6}Si_6O_{26-\delta}$ and $Ca_2Gd_{6.4}Eu_{1.6}Si_6O_{26-\delta}$ bulk phosphors. Along with the narrow luminescence lines from Eu^{3+} ions, there are broad bands $(\lambda_{max} = 443 \text{ nm})$ caused by luminescence of Eu^{2+} ions $(4f^65d \rightarrow 4f'(^8S_{7/2})$ transition). The broad bands have a weak structure, which is likely to be

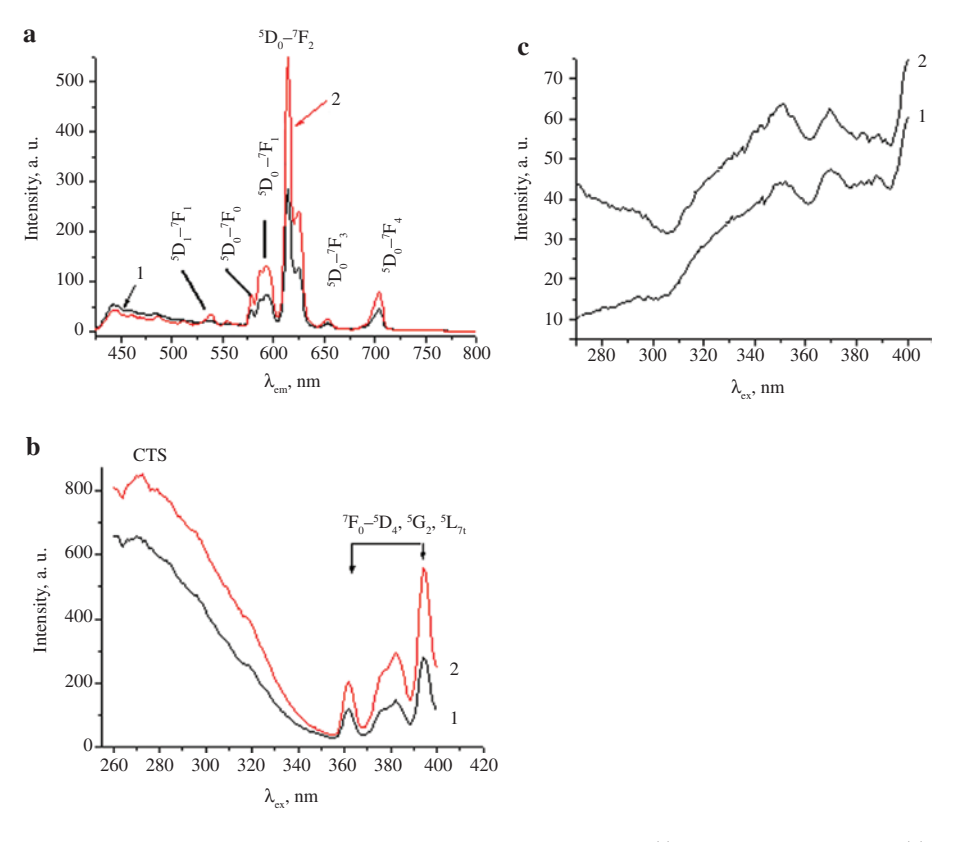


Fig. 11: The PL and PLE spectra of bulk phosphors $Ca_2Y_{6.4}Eu_{1.6}Si_6O_{26-\delta}$ (1) and $Ca_2Gd_{6.4}Eu_{1.6}Si_6O_{26-\delta}$ (2): the PL spectra of samples 1 and 2 (a); the PLE spectra (λ_{em} = 614 nm) (b) and (λ_{em} = 443 nm) of samples 1 and 2 (c).

due to the interaction of the $4f^6$ and 5d electrons [32]. Since during Y(Gd) substitution Eu³⁺ ion occupies two crystallographic positions in the structure of silicates, 4f and 6h, then Eu³⁺ forms two types of optical centers. The spectra are the total luminescence spectra of these two centers.

In our opinion, the mechanism of formation of Eu^{2+} ions can be analogous to that reported in works [13, 33]. During synthesis of $Ca_2Y(Gd)_{6,4}Eu_{1.6}Si_6O_{26-\delta}$ polycrystals, in the process of high-temperature annealing of the mixture of initial components, $V_{ca}^{\prime\prime}$ vacancies are formed in the 4f position of the formed oxyapatite. The $V_{ca}^{\prime\prime}$ vacancies give their negative charge to two Eu_{γ}^{3+} or Eu_{Gd}^{3+} ions. This leads to the formation of Eu^{2+} . Therefore the chemical formula of the samples should be written as $Sr_2Y(Gd)_{6,4}Eu_{1.6}Si_6O_{26-\delta}$, where δ is oxygen nonstoichiometry.

The excitation spectra of bulk phosphors (Fig. 11b) for $\lambda_{\rm em}=614$ nm contain the CTS bands and the lines induced by ${}^7F_0 \rightarrow {}^5D_4$, 5G_2 , 5L_7 transitions. For $\lambda_{\rm em}=443$ nm, the excitation spectra (Eu²+) in the wavelength interval 260–305 nm are different (Fig. 11c). For the III phosphor, the absorption intensity in this wavelength interval increases, in contrast to the II phosphor. The broad bands in the interval 305–390 nm are due to the transition from the $4f^7({}^8S_{7/2})$ level to the e_g level of the 5d state of Eu²+ ions. These broad bands for the both phosphors contain two maxima at ~351 and 369 nm, which are induced probably by splitting of the e_g level [34]. This is indicative of a rather strong interaction between the $4f^6$ electrons and the 5d electron.

Figure 12 demonstrates the PL and excitation spectra of the nanophosphors produced by evaporation of II and III samples in vacuo. The PL spectra are broad bands determined by the luminescence of Eu^{2+} ions. The luminescence of Eu^{3+} ions is quenched almost completely (Fig. 12a). For the nanophosphor obtained by evaporation of the II sample in argon atmosphere the intensity of the ${}^5D_0 \rightarrow {}^7F_{1,2}$ transitions is much smaller than for the analogous sample produced by evaporation in vacuum, while the luminescence intensity of Eu^{2+} ions is greater. It can be supposed that the Eu^{2+} ions are additionally formed in the nanosamples due to

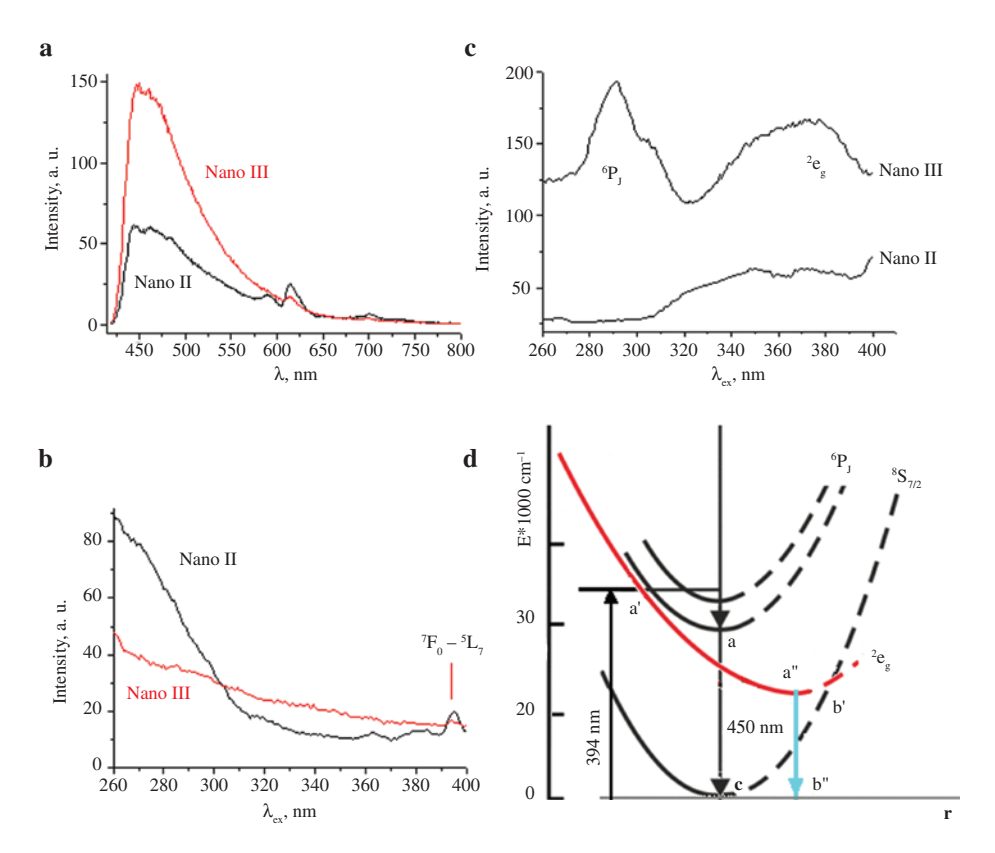


Fig. 12: The PL (a) and PLE (λ_{em} = 614 nm) (b) and (λ_{em} = 443 nm) (c) spectra of the NP produced by evaporation of $Ca_2Y_{6.4}Eu_{1.6}Si_6O_{26-\delta}$ (II) and $Ca_2Gd_{6.4}Eu_{1.6}Si_6O_{26-\delta}$ (III). Scheme for Eu^{2+} ion in configuration coordinates of NP produced by evaporation of sample II (d)

radiation reduction $Eu^{3+} \rightarrow Eu^{2+}$. Thus, the reduction of $Eu^{3+} \rightarrow Eu^{2+}$ ions depends not only on the atmosphere, in which evaporation takes place, but also on the composition of initial bulk samples.

The luminescence intensity of Eu^{2+} ions for $Ca_{_{2}}Y_{_{6,4}}Eu_{_{1,6}}Si_{_{6}}O_{_{26-\delta}}$ and for the nanophosphor produced on its basis is almost the same. We speculate that no $Eu^{3+} \rightarrow Eu^{2+}$ reduction takes place in the sample. The small luminescence yield of Eu³⁺ ions can be explained with the use of the configuration diagram in the Deckster-Click-Russel model [27].

Consider the excitation spectra of the nanophosphors. In the excitation spectra of the nanophosphors (Fig. 12b) for $\lambda_{em} = 614$ nm, the lines determined by the ${}^{7}F_{0} \rightarrow {}^{5}D_{4}$, ${}^{5}G_{2}$, ${}^{5}L_{7}$ transitions have a much lower intensity compared with the excitation spectra of bulk phosphors (Fig. 11b). This confirms a relatively small number of Eu³⁺ ions taking part in the process of luminescence.

For the nanosample based on $Ca_2Y_{6.4}Eu_{1.6}Si_6O_{26-87}$, the Eu^{2+} excitation spectrum (λ_{em} = 443 nm) is almost the same as for the bulk sample, whereas for the nanosample based on $Ca_2Gd_{64}Eu_{16}Si_6O_{26-\delta}$ the 2e_g level becomes degenerated and additional excitation bands appear in the region of 260-320 nm (Fig. 12c). These bands are likely to correspond to the ${}^8S_{7/2} \rightarrow {}^6P_1$ transitions of Eu²⁺ ion. Consequently, during the bulk \rightarrow nano transition the ligand field around Eu²⁺ changes. This can be due (as mentioned above) to translational symmetry violation in the NP. The bonding of the 4f and 5d electrons weakens. The ²e_o level degenerates. The Eu^{2+} ion from the ${}^6P_{_{\rm I}}$ state nonradiatively relaxes into the $e_{_{\rm g}}$ state, from which the luminescence is generated (Fig. 12d).

Figure 12d presents a scheme for Eu2+ ion in configuration coordinates (r) for a nanophosphor based on sample III. The Eu²⁺ ion levels ${}^8S_{7/2}$ and ${}^6P_{_{\rm J}}$ are shown. As a result of excitation of the ${}^6P_{_{\rm J}}$ level, the Eu²⁺ ion exhibits a radiationless relaxation into the ${}^2e_{_{\sigma}}$ state (a \rightarrow a'). Then an a' \rightarrow a" \rightarrow b" transition and radiation with λ^{max} = 450 nm take place. At sufficient temperature, a radiationless transition a' \rightarrow b' \rightarrow c into the ${}^{8}S_{7/2}$ level is also possible.

Optical spectroscopy of selected germanates

Consider the variation in the forbidden band E_g width of samples IV during the transition from bulk powder to NP. Figure 10d demonstrates the absorption spectra of the bulk samples $Ca_2La_{6.4}Eu_{1.6}Ge_6O_{26}$ and NP based thereon. The absorption spectrum of the bulk sample has two bands with maxima at ~246 and 300 nm. These bands are due to a transition into the charge-transfer state for two types of optical centers formed by Eu^{3+} ions in the 4f and 6h positions. For $Ca_2La_{6.4}Eu_{1.6}Ge_6O_{26}$, the absorption band edge is located at ~350 nm, which corresponds to $E_g = 3.5$ eV. In the region of the NP absorption boundary there is an extended exponential tail (Uhrbach tail) typical of amorphous media [31]. The Uhrbach tail does not allow the absorption boundary value to be estimated.

The luminescence and excitation spectra of the bulk sample $\text{Ca}_2\text{La}_{6,4}\text{Eu}_{1,6}\text{Ge}_6\text{O}_{26-\delta}$ are given in Fig. 13a and b. The spectral characteristics of this phosphor have been described in detail in work [14]. The Eu^{3+} ions form two types of optical centers at $\lambda_{\text{max}} = 577.4$ and 578 nm. For the $\text{Ca}_2\text{La}_{6,4}\text{Eu}_{1,6}\text{Ge}_6\text{O}_{26-\delta}$ based nanosample, the luminescence spectrum changes considerably (Fig. 13c). Luminescence appears in the interval 450–750 nm ($\lambda_{\text{ex}} = 394$ nm), which is due to Eu^{2+} ions. The mechanism of formation of Eu^{2+} ions, in our opinion, is analogous to that for the nanophosphors based on samples II and III: radiation reduction $\text{Eu}^{3+} \to \text{Eu}^{2+}$. The luminescence spectrum of Eu^{2+} ions demonstrated in Fig. 13c is decomposed into two Gauss components (not shown in Fig. 13c) with $\lambda_{\text{max}} = 455.4$ and 582.2 nm. Consequently, the Eu^{2+} ion forms two types of optical centers, probably, in the 4f and 6h positions. Figure 13d displays the nanophosphor excitation spectrum ($\lambda_{\text{em}} = 443$ nm). A broad band ($447-44^650^4$ transition of Eu^{2+} ions) and lines corresponding to f–f transitions of Eu^{3+} ions are observed in the spectrum. The shape of the spectrum is indicative of the resonant interaction between Eu^{2+} and Eu^{3+} ions.

The radiation of Eu³⁺ ions is superimposed on the luminescence spectrum of Eu²⁺ ions. For the 5D_0 – 7F_2 transition, the most intense lines are observed at 615 and 623 nm. For the bulk sample, the lines of this transition are observed at 613 and 620 nm. It is known that the electric dipole transition $^5D_0 \rightarrow ^7F_2$

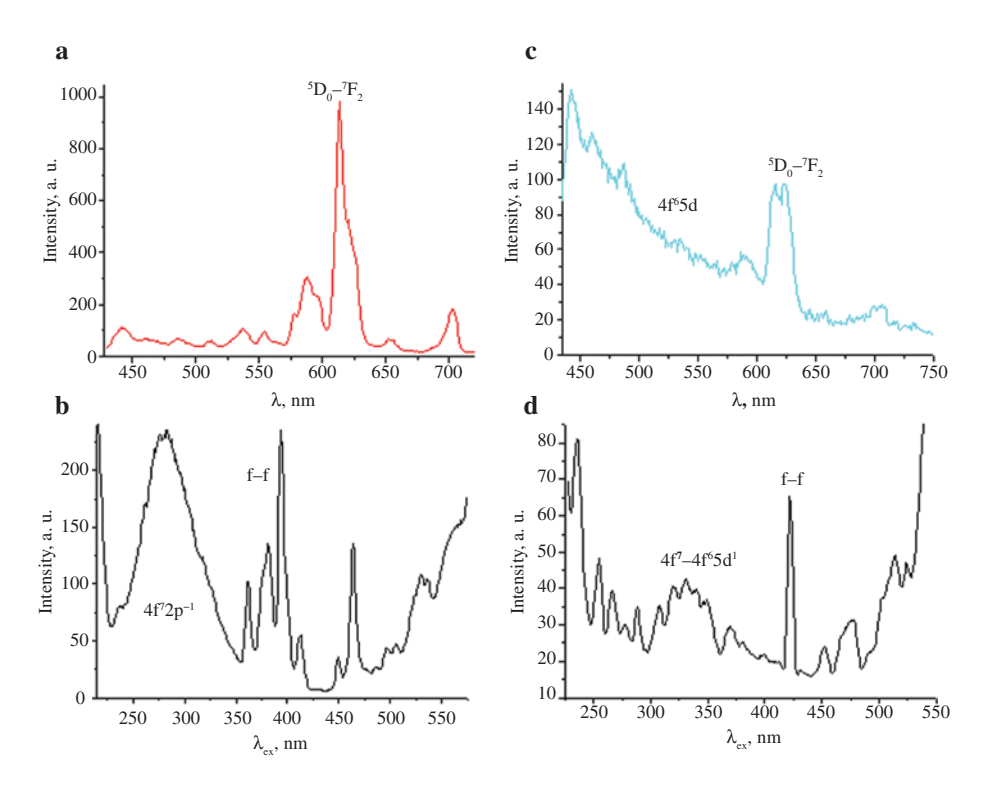


Fig. 13: The PL spectra of phosphors $Ca_2La_{6.4}Eu_{1.6}Ge_6O_{26-\delta}$ (IV) (a), NP (c) and the PLE spectra ($\lambda_{em}=614$ nm) of samples IV (b), NP ($\lambda_{em}=443$ nm) (d).

is supersensitive to the site-symmetry of Eu³⁺ ion in the optical center. The shift of the transition lines in the NP towards higher energies and the redistribution of their relative intensities suggest a certain distortion of the local environment of Eu³⁺ ions in the nanophosphor compared with the bulk phosphor, which is likely to be due to partial polymerization of GeO, tetrahedra and to the formation of Ge-O-Ge bridges. The superposition of Eu²⁺ and Eu³⁺ ion radiation generates white luminescence of the phosphor with color coordinates x = 0.313, y = 0.320.

Conclusions

Amorphous nanophosphors have been produced for the first time by electron beam evaporation of bulk phosphors of REE silicates and germinates activated with europium. The processes of crystallization of amorphous nanophosphors have been studied by differential scanning calorimetry and thermogravimetry methods. The spectral and luminescence characteristics of phosphors in the polycrystalline and nanoamorphous states have been investigated. A modification of the Raman and IR spectra was found when the particle size decreases from bulk to nanostate owing to insignificant polymerization of SiO, and GeO, tetrahedra in the NP. When going from bulk to NP, the value of E_o increases. New red, blue and white amorphous nanophosphors have been obtained. Radiation reduction of ions $Eu^{3+} \rightarrow Eu^{2+}$ in electron beam has been presumably found.

Acknowledgments: The authors are grateful to Dr. I. V. Baklanova for their assistance in recording Raman, IR and PL spectra.

References

- [1] L. Boyer, B. Piriou, J. Carpena, J. L. Lacout. J. Alloys Comp. 311, 143 (2000).
- [2] B. Chu, C. Guo, Q. Su. Mater. Chem. Phys. 84, 279 (2004).
- [3] G. S. R. Raju, H. C. Jung, J. Y. Park, B. K. Moon, R. Balakrishnaiah, J. H. Jeong, J. H. Kim. Sens. Actuat. B. 146, 395 (2010).
- [4] C. Peng, G. Li, Z. Hou, M. Shang, J. Lin. Mater. Chem. Phys. 136, 1008 (2012).
- [5] F. Flory, L. Escoubas, G. Berginc. J. Nanophotonics. 5, 052502 (2011).
- [6] Nanophotonics-foresight-report-june-2011. Report eds. N. van Hulst, S. Kennedy. ICFO-The Institute of Photonic Sci. Barcelona, Spain. www.nanophotonic-foresight- report-june-(2011).
- [7] M. G. Zuev, S. Yu. Sokovnin, V. G. Il'ves, I. V. Baklanova. RU Patent 2 579 135, Filed 09 Dec 2014, Issued 27 March (2016).
- [8] S. Yu. Sokovnin, V. G. Il'ves. Application of a pulse Electron Beam for Receiving Nanopowders of Some Metall Oxides, p. 94. RIO Ural Branch RAS, Yekaterinburg (2012).
- [9] L. C. Leu, S. Thomas, M. T. Sebastian, S. Zdzieszynski, S. Misture, R. Ubicz. J. Am. Ceram. Soc. 94, 2625 (2011).
- [10] M. G. Zuev, V. G. Il'ves, S. Yu. Sokovnin, A. V. Spirina. Izvestiya vuz. Fizika. 55(12/3), 223 (2012).
- [11] S. Thomas. Silicate and Aluminate Based Dielectric Ceramics for Microwave Communication. Under the Guidance and Supervision of Dr. M.T. Sebastian (Supervisor). National Institute for Interdisciplinary Science and Technology (CSIR), Thiruvananthapuram (2010).
- [12] S. Yu. Sokovnin, V. G. Il'ves, M. G. Zuev. "Production of complex metal oxide nanopouders using pulsed electron beam in low-pressure gas for biomaieriats application" Chapter 2, in Engineering of Nanobiomaterials Applications of Nanobiomaterials, A. Grumezescu (Ed.), vol. 2, p. 29, Elsevier, Oxford (2016).
- [13] M. G. Zuev, S. Yu. Sokovnin, V. G. Il'ves, I. V. Baklanova, A. A. Vasin. J. Solid State Chem. 218, 164 (2014).
- [14] A. A. Vasin, M. G. Zuev, E. V. Zabolotskaya, I. V. Baklanova, L. A. Akashev, R. F. Sammigulina. J. Luminescence. 168, 26 (2015).
- [15] S. Brunauer. Adsorbtsiya gazov i parov. Tom 1. Fizicheskaya adsorbtsiya (The Adsorption of Gases and Vapors. Vol. 1. Physical adsorption). Izdatinlit, Moscow (1948).
- [16] Y. Masubuchi, M. Higuchi, T. Takeda, S. Kikkawa. Solid State Ionics. 177, 263 (2006).
- [17] A. N. Lazarev, A. P. Mirgorodskii, I. S. Ignat'ev. Vibrational Spectra of Complex Oxides, p. 211. ([in Russian]) Nauka, Leningrad (1975).
- [18] Yu. K. Voron'ko, A. A. Sobol', V. E. Shukshin, A. I. Zagumennyi, Yu. D. Zavartsev, S. A. Kutovoi. Phys. Solid State. 54, 1635 (2012).

- [19] C. Y. Xu, P. X. Zhang, L. Yan. J. Raman Spectrosc. 32, 862 (2001).
- [20] K. Rout, M. Mohapatra, S. Anand. Appl. Surf. Sci. 270, 205 (2013).
- [21] O. S. Ken, D. A. Andronikov, D. A. Yavsin, A. V. Kukin, S. N. Danilov, A. N. Smirnov, O. M. Sreseli, S. A. Gurevich. Semiconductors. 48, 1518 (2014).
- [22] T. F. Tenisheva, A. N. Lazarev, T. M. Pavlyukevich. Bull. of the Academy of Sci. of the USSR, Division of chemical sci. 14, 1520 (1965).
- [23] E. Rodríguez-Reyna, A. F. Fuentes, M. Maczka, J. Hanuza, K. Boulahya, U. Amador. Solid State Sci. 8, 168 (2006).
- [24] E. J. Baran, C. Cascales. J. Raman Spectrosc. 30, 77 (1999).
- [25] A. M. Karpov, M. G. Zuev. Glass Phys. Chem. 38, 431 (2012).
- [26] R. S. Yadav, R. K. Dutta, M. Kumar, A. C. Pandey. J. Luminescence. 129, 1078 (2009).
- [27] G. Blasse, A. Bril. Philips Techn. Rev. 31, 304 (1970).
- [28] C. R. Ronda, T. Jüstel, H. Nikol. J. Alloys Comp. 275-277, 669 (1998).
- [29] M. I. Gaiduk, V. F. Zolin, L. S. Gaigerova. Luminescencse Spectra of Europium, p. 75. [in Russian] Nauka, Moscow (1974).
- [30] I. A. Belova, F. A. Bol'shchikov, Yu. K. Voron'ko, A. V. Malov, A. V. Popov, P. A. Ryabochkina, A. A. Sobol', S. N. Ushakov. Phys. Solid State. 50, 1611 (2008).
- [31] I. A. Vainshtein, A. F. Zatsepin, V. S. Kortov, Yu. V. Shchapova. Phys. Solid State. 42, 230 (2000).
- [32] F. M. Ryan, W. Lehmann, D. W. Feldman, J. Murphy. J. Electrochem. Sac. Solid-state Sci. Technol. 121, 1475 (1974).
- [33] M. G. Zuev, A. M. Karpov, A. S. Shkvarin. J. Solid State Chem. 184, 52 (2011).
- [34] M. G. Zuev, V. G. Il'ves, S. Yu. Sokovnin, I. V. Baklanova, A. A. Vasin, E. Yu. Zhuravleva. J. Luminescence. 188, 31 (2017).